Localized spin-orbit polaron in magnetic Weyl semimetal Co3Sn2S2

Yuqing Xing
Institute of Physics, Chinese academy of sciences https://orcid.org/0000-0002-8646-6631
Jianlei Shen
Institute of Physics, Chinese academy of sciences
Hui Chen
Institute of Physics, Chinese Academy of Sciences
Li Huang
Institute of Physics, Chinese Academy of Sciences
Yuxiang Gao
Institute of Physics, Chinese academy of sciences
Qi Zheng
Institute of Physics, Chinese Academy of Sciences
Yu-Yang Zhang
University of Chinese Academy of Sciences, Chinese Academy of Sciences https://orcid.org/0000-0002-9548-0021
Geng Li
Institute of Physics & University of Chinese Academy of Sciences, Chinese Academy of Sciences https://orcid.org/0000-0002-3347-7222
Bin Hu
Institute of Physics, Chinese academy of sciences
Guojian Qian
Institute of Physics, Chinese academy of sciences
Lu Cao
Beijing National Laboratory for Condensed Matter Physics and Institute of Physics, Chinese Academy of Sciences https://orcid.org/0000-0001-9549-8136
Xianli Zhang
Institute of Physics, Chinese academy of sciences
Peng Fan
Institute of Physics, Chinese Academy of Sciences
Ruisong Ma
Institute of Physics, Chinese Academy of Sciences
Qi Wang

Department of Physics and Beijing Key Laboratory of Opto-electronic Functional Materials & Micro-nano Devices, Renmin University of China

Qiangwei Yin
Renmin University of China

Hechang Lei
Renmin University of China https://orcid.org/0000-0003-0850-8514

Wei Ji
Department of Physics and Beijing Key Laboratory of Optoelectronic Functional Materials & Micro-Nano Devices, Renmin University of China, Beijing 100872 https://orcid.org/0000-0001-5249-6624

Shixuan Du
Chinese Academy of Sciences and Songshan Lake Materials Laboratory

Haitao Yang
Institute of Physics and University of Chinese academy of sciences

Chengmin Shen
Institute of Physics, Chinese Academy of Sciences

X. Lin
Institute of Physics & University of Chinese Academy of Sciences, Chinese Academy of Sciences

Enke Liu
Institute of Physics https://orcid.org/0000-0002-5498-993X

Baogen Shen
Institute of Physics of Chinese Academy of Sciences

Ziqiang Wang
Boston College

Hong-Jun Gao (hjgao@iphy.ac.cn)
Institute of Physics https://orcid.org/0000-0001-9323-1307

Article

Keywords:

Posted Date: August 13th, 2020

DOI: https://doi.org/10.21203/rs.3.rs-53173/v1

Version of Record: A version of this preprint was published at Nature Communications on November 5th, 2020. See the published version at https://doi.org/10.1038/s41467-020-19440-2.

Localized spin-orbit polaron in magnetic Weyl semimetal $Co_3Sn_2S_2$

Yuqing Xing[1,2,3†], Jianlei Shen[1,2†], Hui Chen[1,2,3†], Li Huang[1,2,3†], Yuxiang Gao[1,2,3], Qi Zheng[1,2,3], Yu-Yang Zhang[2,3], Geng Li[1,2,3], Bin Hu[1,2,3], Guojian Qian[1,2,3], Lu Cao[1,2,3], Xianli Zhang[1,2,3], Peng Fan[1,2,3], Ruisong Ma[1,2,3], Qi Wang[4], Qiangwei Yin[4], Hechang Lei[4], Wei Ji[4], Shixuan Du[1,2,3,5], Haitao Yang[1,2,3], Chengmin Shen[1,2,3], Xiao Lin[2,1,3], Enke Liu[1,2,5], Baogen Shen[1,2], Ziqiang Wang[6*], and Hong-Jun Gao[1,2,3,5*]*

[1] *Beijing National Center for Condensed Matter Physics and Institute of Physics, Chinese Academy of Sciences, Beijing 100190, PR China*

[2] *School of Physical Sciences, University of Chinese Academy of Sciences, Beijing 100190, PR China*

[3] *CAS Center for Excellence in Topological Quantum Computation, University of Chinese Academy of Sciences, Beijing 100190, PR China*

[4] *Beijing Key Laboratory of Optoelectronic Functional Materials & Micro-Nano Devices, Department of Physics, Renmin University of China, Beijing 100872, PR China*

[5] *Songshan Lake Materials Laboratory, Dongguan, Guangdong 523808, PR China*

[6] *Department of Physics, Boston College, Chestnut Hill, MA, USA*

†These authors contributed equally to this work

[*]Correspondence to: hjgao@iphy.ac.cn, wangzi@bc.edu, ekliu@iphy.ac.cn

The kagome lattice $Co_3Sn_2S_2$ exhibits the quintessential topological phenomena of a magnetic Weyl semimetal such as the chiral anomaly and Fermi-arc surface states. Probing its magnetic properties is crucial for understanding this correlated topological state. Here, using spin-polarized scanning tunneling microscopy/spectroscopy (STM/S) and non-contact atomic force microscopy (nc-AFM) combined with first-principle calculations, we report the discovery of localized spin-orbit polarons (SOPs) with three-fold rotation symmetry nucleated around single S-vacancies in $Co_3Sn_2S_2$. The SOPs carry a magnetic moment and a large diamagnetic orbital magnetization of a possible topological origin associated relating to the diamagnetic circulating current around the S-vacancy. Appreciable magneto-elastic coupling of the SOP is detected by nc-AFM and STM. Our findings suggest that the SOPs can enhance magnetism and more robust time-reversal-symmetry-breaking topological phenomena. Controlled engineering of the SOPs may pave the way toward practical applications in functional quantum devices.

As a magnetic Weyl semimetal[1–4], $Co_3Sn_2S_2$ integrates the flat bands of correlated *d*-electrons on the kagome lattice[5–7] into the topological electronic structure[8–11] and exhibits remarkably novel phenomena such as the giant anomalous Hall/Nernst effect[8,12], chiral-anomaly[8], surface-termination dependent Fermi arcs[11], topological catalysis[13], flat band Berry phase and orbital magnetization[14]. While magnetism plays a fundamental role in driving these intriguing properties by breaking the time-reversal symmetry, the magnetic properties of localized excitations around atomic defects in magnetic Weyl semimetals have not been explored. Probing the nature of the defect excitations can provide a deeper understanding of the physics of correlated topological materials and the control of emergent quantum states via manipulations of magnetic order[15–17].

Here, we study localized magnetic polarons nucleated around single atomic S vacancies on S-terminated surface in $Co_3Sn_2S_2$ by spin-polarized STM. They emerge as bound states in the conductance map with a three-fold rotation symmetry. Applying external magnetic fields up to ±6 T normal to the surface reveals that the binding energy of the localized magnetic polaron linearly increases as a function of the field magnitude regardless of the field direction. This anomalous Zeeman response of a magnetic bound state has not been observed before and indicates dominant orbital magnetization contribution to the local magnetic moment (~ 1.35 μ_B). Appreciable magneto-elastic coupling is also detected near the S-vacancy. We term this new excitation as a localized spin-orbit polaron (SOP) and argue that the large orbital magnetization has a topological origin associated with the Berry phase and the persistent circulating current due to the magnetoelectric effect of the topological magnet.

$Co_3Sn_2S_2$ has a layered structure which consists of two hexagonal planes of S and Sn as well as a Co_3Sn kagome layer sandwiched between the S atoms (Fig. 1a). The magnetic Weyl semimetal has a Curie temperature of 177 K and a low-temperature out of the plane magnetic moment of about 0.3 μ_B/Co[9,18,19]. We employ spin-polarized STM/S to study the cleaved surface of $Co_3Sn_2S_2$ (Fig. 1b). In STM topographic images, two types of cleaved surfaces were observed. Type-I surfaces show a hexagonal-like lattice with randomly distributed vacancies (Fig. 1c), while Type-II surfaces show a similar hexagonal-like lattice with adatoms and clusters (Fig. 1e).

Weak bonds between S and Sn atoms offer a cleave plane and possibly lead to S-terminated and Sn-terminated surfaces. It is crucial to distinguish the two types of surfaces of the cleaved sample, which has been a controversial issue in previous studies[11,14,20,21]. In order to further identify the two surfaces, we conducted the local contact potential difference (LCPD) measurement on both surfaces using the low-

temperature (4.5 K) nc-AFM/STM, which is based on a qPlus sensor[22]. Typical STM images of the Type-I and Type-II surfaces of $Co_3Sn_2S_2$ show the hexagonal lattice, with distinctive features of randomly distributed vacancies for Type-I surface and bright dots for Type-II surface. Zoomed-in nc-AFM images (Fig. 1d and Fig. 1f) of the two surfaces show consistent topography with the corresponding STM images. We then investigate the LCPD on the two surfaces by measuring frequency shift (Δf) with respect to the sample bias V (Fig. 1g), respectively[23]. On the Type-I surface, the maximum of the parabola in the obtained $\Delta f(V)$ is V^{I}_{CPD} = -0.22 V, and on the Type-II surface, V^{II}_{CPD} = +0.57 V, which indicate that the work function of Type-I surface is ~ 0.79 eV higher than that of Type-II surface (Extended Data Fig. 1)[24]. In addition, we calculated the work functions of the S (5.29 eV) and Sn (4.34 eV) terminated surfaces, respectively. The calculated work function value on the S-terminated surface is 0.95 eV higher than that on the Sn-terminated surface. This clearly demonstrates that the surface with the higher work function (Type-I surface) is the S-terminated surface.

We next studied the properties of localized excitations by focusing on a region with S vacancies on the S-terminated surface. A large-scale topographic image shows randomly distributed S vacancies of the focused region (Fig. 2a) and a zoomed-in image depicts a single S-vacancy (Fig. 2c). A typical off-vacancy dI/dV spectrum (black curve in Fig. 2b) closely resembles the one taken in a region free of S vacancies on the S-surface, exhibiting an energy range of suppressed and flat density of states of about 300 meV[11,20], and a broad hump around +50 meV, which originates from the topological surface states of the $Co_3Sn_2S_2$ magnetic Weyl semimetal[11,20]. There is also a peak sitting at the edge of the valence band at -350 meV. Differently, the dI/dV spectrum taken at the S-vacancy (orange curve in Fig. 2b) shows suppressed density of states around +50 meV and -350 meV. Meanwhile, a series of approximately equal-spaced spectral peaks emerge just above the valence band inside the region of suppressed density of states, indicating bound states formation at the S-vacancy. From statistical analysis, we determine the average energy spacing between the spectral peaks to be ~16 meV (Extended Data Fig. 2). Spatial distributions of these spectroscopic features were recorded in dI/dV maps (Fig. 2d-h and Extended Data Fig. 3). The conductance map at +50 mV (Fig. 2d) shows an atomically modulated scattering pattern of the low-energy surface states at the S-vacancy. The map acquired at -350 mV (Fig. 2e) reveals a three-fold structure with suppressed intensity around the S-vacancy and all its six neighboring S atoms. Remarkably, the conductance maps (Fig. 2f-h) recorded at those three discernable dI/dV peaks, i.e. at -322, -300, and -283 mV, all show localized flower-petal shaped patterns. Each pattern exhibits a three-fold rotation symmetry

centered at the S-vacancy and the boundary of the pattern reaches as far as the six neighboring S atoms, which approximately defines the size of the bound states (Fig. 2i).

The peak residing at -283 mV (Fig. 2b) is the sharpest and the most localized one, which is referred to the primary bound state. It consists of two sub-peaks with small energy splitting (Extended Data Fig. 4). The brightest portion of its intensity is distributed over the three up-triangles closest to the vacancy, one in each of the three petals, in the underlying kagome lattice (highlighted by the red up-triangles in Fig. 2h), clearly demonstrating the driving force for the formation of the bound state polaron is the localization of the Co *d*-electrons by the vacancy potential of the missing S^{2-} ion, which hybridize with the S *p*-electrons. Interestingly, the conductance map of the -283 mV state (Fig. 2h), also those of the -322 and -300 mV states (Fig. 2f and 2g), show a dramatic contrast/intensity reversal in comparison with the map of the -350 mV state (Fig. 2e), suggesting the -350 mV state be an antibound state, an affirmation of the bound state nature of the S-vacancy induced polaron. A ~67 meV energy separation between the bound and antibound states allows us to estimate the "bandwidth" of the polaronic state.

To investigate the magnetic properties of the bound states, we used spin-polarized Ni tips to measure dI/dV spectra on the single S-vacancy (Fig. 1b). The spin-polarization of the Ni tip was calibrated on Co/Cu(111) (Extended Data Fig. 5). An external magnetic field of +0.6 T (-0.6 T) was applied to magnetize the Ni tip to be in the spin up (spin down) state. This tip was then used to measure the spin-dependent dI/dV spectra at 0 T. We did not observe appreciable spin-polarized contrast in any defect-free regions of the S-terminated surface, indicating that the intact S-terminated surface is nearly non-magnetic (Fig. 3a and Extended Data Fig. 6). At the S-vacancy, the dI/dV spectra, however, show strong magnetic contrast from approximately -350 mV to -280 mV where the bound states reside, indicating that the bound states are magnetic with a spin-down majority (Fig. 3b).

Figure 3c shows the spin flip operation of the Ni tip[25,26], where we zoomed in to more closely show the primary bound state at ~ -283 mV (marked by the black arrow in Fig. 3b). Particularly, a spin-down tip was initially prepared, which gave a pronounced peak around -283 mV (left panel in Fig. 3c). The polarization of the tip was then flipped to spin-up by an external magnetic field of +0.6 T. Given this tip, the intensity of the -283 mV peak reduces while the peak position keeps unchanged (middle panel in Fig. 3c). After flipping the tip spin back to spin-down, the peak intensity restores (right panel in Fig. 3c). This result demonstrates that the bound states are magnetic polarons introduced by the S vacancies (Extended Data Fig. 7).

We further investigated the nature of the localized magnetic polaron by measuring the magnetic field response of the spectral peaks using a normal W tip. The field is applied perpendicularly to the sample surface, ranging from -6 T to 6 T. The energies of the both sub-peaks of the primary bound state shift linearly toward the higher energy side ($\Delta E > 0$), *independent of the direction of the magnetic field* (Fig. 4a-b). This unusual behavior is reproducible on various individual S vacancies (Extended Data Fig. 8). The Zeeman effect $\Delta E = -\vec{\mu} \cdot \vec{H}$ indicates that the energy of a polarized (nondegenerate) magnetic state would decrease if the magnetic moment ($\vec{\mu}$) was parallel to the applied field but would increase if it was oriented antiparallel. The observed anomalous Zeeman response has two important physical implications. A ΔE independence of field directions implies that the magnetic field couples to the magnetization of the bound state, which simultaneously flips upon reversing the field direction. In addition, $\Delta E > 0$ indicates that the net magnetization is always oriented antiparallel to the direction of the magnetic field, indicative of a dominant diamagnetic orbital current contribution, in addition to the pseudospin (electron spin + atomic orbital) contribution in the presence of spin-orbit coupling.

To emphasize its orbital magnetic moment, we dub the magnetic bound state as a localized spin-orbit polaron (SOP). Fitting the two sub-peak positions as a linear function of the magnetic field (Fig. 4c), we obtained a slope of 75 μeV/T = 1.35 μ_B for the effective magnetic moment of the SOP. The anomalous Zeeman response was recently observed for the flat portion of the itinerant band states corresponding to a peak in the density of states at low energies and attributed to the Berry phase induced orbital magnetization[14]. A crucial difference of the previous work from the present lies in that the energy shift confined to the flat part of the band states does not correspond to a net magnetic moment and the orbital magnetization averages out to approximately zero when all momentum states are considered[14]. The anomalous Zeeman shift observed here, however, comes from a localized bound state and corresponds to the overall magnetic field response of a net physical magnetic moment. The large orbital magnetization of the SOP most likely originates from the persistent circulating current around the S-vacancy due to the Berry phase and magnetoelectric effect of the topological Weyl semimetal[27].

The possible origin of the orbital magnetization of the SOP is new and intriguing. In dilute magnetic semiconductors (DMS)[28,29] such as (Ga, Mn)As, the doped magnetic ion Mn^{2+} induces a magnetic polaron through the exchange coupling to the weakly correlated itinerant *p*-orbital electrons in the hole-band with spin-orbit coupling. While direct measurements of the magnetic properties of an isolated Mn^{2+} are not available, the orbital contribution was estimated theoretically to dominate over the spin contribution to the

hole magnetization[30], which is nevertheless too small (~ 5%) compared to the saturated FM moment. The orbital magnetic moment was thus not crucial for DMS, although the physics of bound magnetic polarons[31–33] plays an important role in producing the FM order.

The physics in the topological Weyl semimetal $Co_3Sn_2S_2$ is different and much richer. First of all, the transition metal Co dominates both the itinerant and localized magnetism. The itinerant electrons come from the correlated Co 3*d* orbitals mixed with the Sn and S *p*-orbitals on the kagome lattice with frustrated kinetic energy[34]. The flat bands and the strong spin-orbit coupling endow the conduction electrons with robust spin-polarization and Berry phase. The "dopant" here is a S^{2-} vacancy residing out of the Co kagome lattice plane that causes the localization of the magnetic Co 3*d* electrons, forming a bound state SOP involving a cluster of atoms (Fig. 2i). It is known theoretically that the Berry phase and orbital magnetization can be established on electronic states localized on atomic clusters[35]. Thus the spin-polarized *d*-electrons naturally contribute to the orbital magnetization of the localized SOP, while the weakly correlated *p*-electrons and the *p*-*d* exchange and charge transfer interactions play a minor role.

Second, more intriguingly, the topological properties of the Weyl semimetal can lead to the large orbital magnetization of the SOP through the magnetoelectric effect of the Weyl fermions. In a 3D strong topological insulator (TI), the Dirac fermion topological surface states, exchange-coupled to a magnetic impurity, produce persistent loop currents with large orbital magnetization around the local moment due to the magnetoelectric effect[36]. Moreover, in 2D TI quantum dots of nanometer sizes, the circulating spin edge currents can be turned into charge current by a time-reversal symmetry breaking magnetic field and produce large orbital magnetization[37]. In magnetic Weyl semimetals, the time-reversal symmetry is intrinsically broken and the surface states carry a well-defined chirality that is robust against disorder and localization[38]. Propagating chiral edge modes have recently been observed at step-edges on the surface of $Co_3Sn_2S_2$[21]. Thus, our experimental findings are consistent with the picture that the spin-polarized localized states generate persistent circulating diamagnetic currents and large orbital magnetization around the S-vacancy, which acts as a magnetic (anti-)dot extending to the neighboring S atoms. Most recently, such circulating persistent currents induced by the topological surface states with diamagnetic moment around quantum dots in Weyl semimetals were theoretically predicted[27], which provides further and more direct support for our experimental findings and theoretical interpretation of the S-vacancy as a quantum dot.

In this sense, the localized SOP in the magnetic Weyl semimetal has an inherent topological origin. While in-depth theoretical works are clearly necessary to account for the rich physics revealed by our experiments, some of the aspects can be captured qualitatively by DFT calculations with spin-orbit coupling, where the total magnetic moment and its orbital content can be studied (Extended Data Fig. 7).

We further considered the magneto-elastic coupling within the localized SOP. The lattice distortion around the S vacancies measured by STM (Fig. 4d) and nc-AFM (Fig. 4e) shows appreciable local atomic displacements at 0 T. The measured average nearest atomic distances around the S-vacancy determine the local atomic displacement ratio as its percentage change from the average distance of an intact region. The displacement ratio significantly decreases with increasing strength of the field applied along the *c*-axis (Extended Data Fig. 9). Remarkably, one-third of the displacement ratio can be manipulated by a magnetic field up to 6 T. These observations further support the SOP nature of the bound states and the strong magneto-elastic coupling in $Co_3Sn_2S_2$.

The discovery of the localized SOP (Fig. 4f) opens a novel route for manipulating the magnetic order and the topological phenomena in Weyl semimetal $Co_3Sn_2S_2$. The STM observed S vacancies on S-terminated surfaces cleaved at low temperature (6 K) indicate the presence of bulk S vacancies, where localized SOPs are expected to nucleate with similar physical properties. DFT calculations reveal that the bulk vacancies are magnetic and significantly enhance the magnetic moment of neighboring Co atoms (Extended Data Fig. 10). The overall density of the SOP can thus be controlled by varying the S pressure and temperature during sample synthesis[39]. In light of this, the enhanced FM moment, experimentally observed with increasing S deficiency in the bulk[39], is most likely a consequence of the nucleation of the magnetic polarons at the S vacancies. A higher SOP density ramps up the scattering of the carriers by the spin-orbit exchange field as well as the exchange interaction between the SOPs, unleashing the potential for more robust time-reversal-symmetry-breaking topological phenomena such as the anomalous Hall and Nernst transport at higher temperatures. Given the role of magnetic dopants in dilute magnetic semiconductors[31–33,35], the vacancy-induced SOP may provide a new path toward generating large magnetic moments in correlated nonmagnetic topological semimetals. Similar to the single defect engineering for scalable qubits and spin sensors in diamond[40], controlled engineering of the SOPs may pave the way toward practical applications in functional quantum devices.

Figure 1

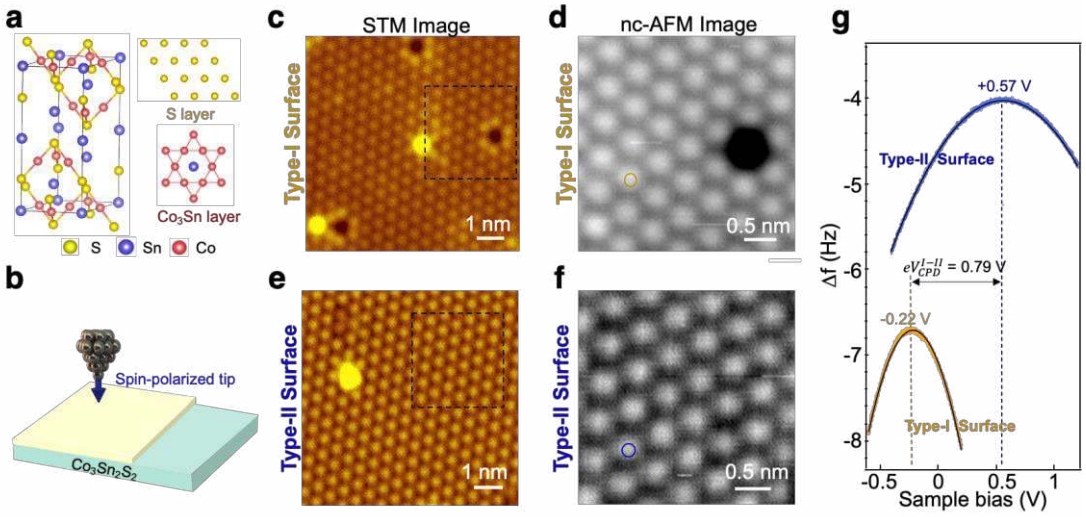

Fig. 1. Identification of S-surface of $Co_3Sn_2S_2$ using nc-AFM/STM. **a,** Atomic structure of $Co_3Sn_2S_2$. **b**, Schematic of spin-polarized STM measurements. **c** and **e,** STM images on Type-I and Type-II surfaces, respectively. **d** and **f,** Zoomed-in nc-AFM images of (**a**) and (**c**) marked by black squares, respectively. **g,** $\Delta f(V)$ curves on the orange and blue circles in (**d**) and (**f**). The maxima of the $\Delta f(V)$ parabolas are located at -0.22 V and +0.57 V for Type-I and Type-II surfaces, respectively. The work function difference between the two surfaces is 0.79 eV (refer to Extended Data Fig. 1 for more information). (STM scanning parameters: bias: V_s= -400 mV, setpoint: I_t= 10 pA); AFM scanning parameters: amplitude= 100 pm, frequency shift Δf = -10 Hz for **d** and -40 Hz for **f**).

Figure 2

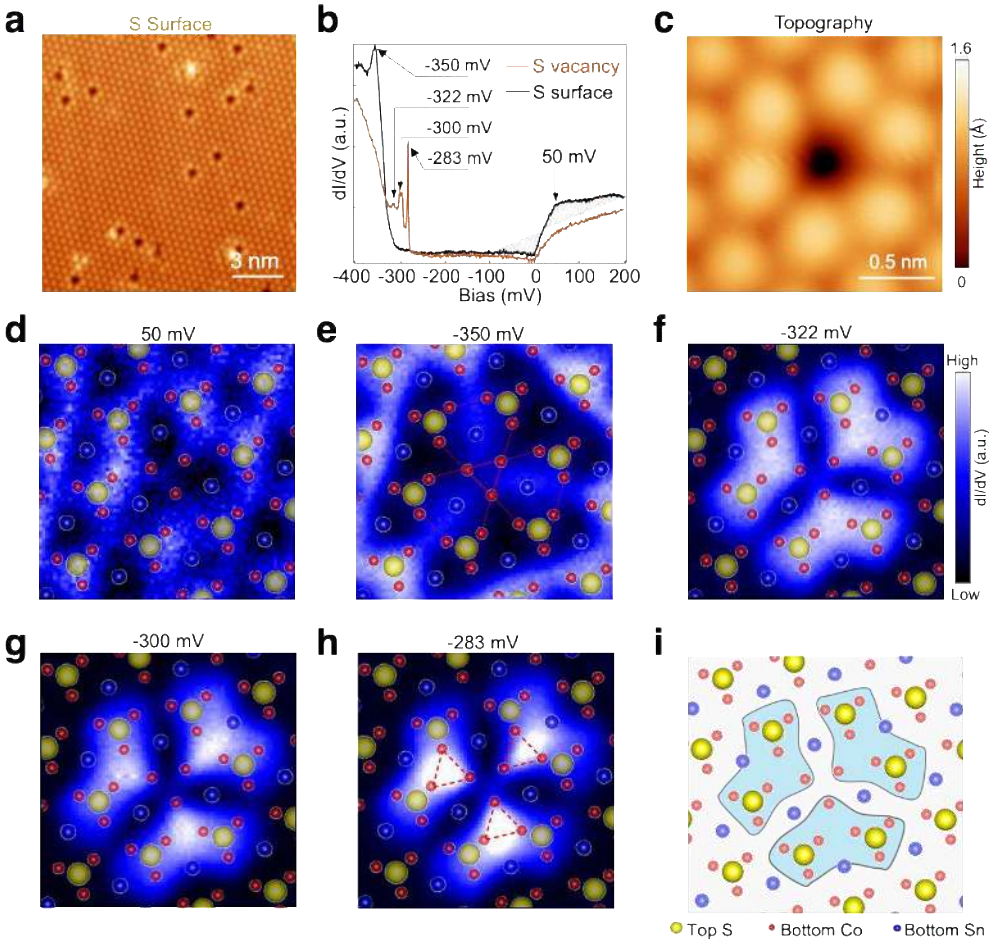

Fig. 2 | Localized excitations around a single S-vacancy at the S-terminated surface of $Co_3Sn_2S_2$. a, Atomic-resolution STM image of the S-terminated surface, showing randomly distributed single vacancies (scanning setting: bias: V_s=-400 mV, setpoint I_t=100 pA). **b,** dI/dV spectra at (orange curve) and off (black curve) a single S-vacancy (V_s=-400 mV, I_t=500 pA, V_{mod}=0.5 mV). **c,** An STM image of a S-vacancy (V_s=-400 mV, I_t=500 pA). **d-h,** dI/dV maps of (**c**) at different energies: 50 meV (**d**), -350 meV (**e**), -322 meV (**f**), -300 meV (**g**), and -283 meV (**h**), respectively. Atomic structure of $Co_3Sn_2S_2$ is overlaid on each map, showing the correlation between the atomic structure and pattern in dI/dV map (V_s=-400 mV, I_t=500 pA, V_{mod}=0.5 mV). **i,** Correlation between the atomic structure and the pattern in the dI/dV map in (**h**), showing that the spatial distribution of bound states is correlated to the underlying Co atoms.

Figure 3

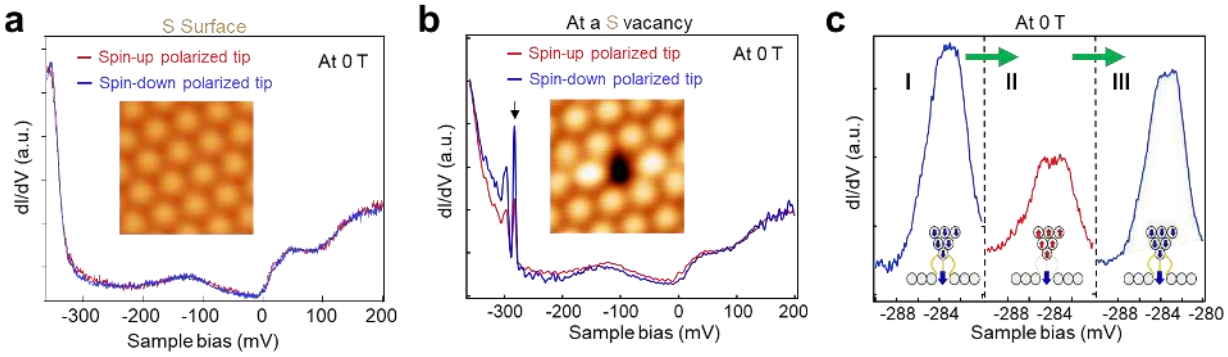

Fig. 3 | Spin-polarized bound states at a single S-vacancy. a, Spin-polarized dI/dV spectra at the vacancy-free region on S-terminated surface using up-polarized tip (red curve) and down-polarized tip (blue curve), showing nearly no polarization contrast on pristine S-termined surface (V_s=-400 mV, I_t=100 pA, Modulation V_{mod}= 0.5 mV). The inset shows the STM image (2 nm × 2 nm) of pristine S-terminated surface. **b,** dI/dV spectra at the center of a single S-vacancy, showing a spin-down majority behavior. The inset shows the STM image (2 nm × 2 nm) of the single S-vacancy (V_s=-400 mV, I_t=200 pA, V_{mod}=0.5 mV). **c,** Spin-flip operation of the STM tip and the reproducible spectra at the S vacancy site. Left curve (curve I) corresponds to the initial spin-down tip polarization, the middle one (curve II) corresponds to spin-up tip polarization induced by a magnetic field, and the right one (curve III) corresponds to flipping the spin of the tip back to the initial spin-down polarization. (V_s=-400 mV, I_t=500 pA, V_{mod}=0.5 mV).

Figure 4

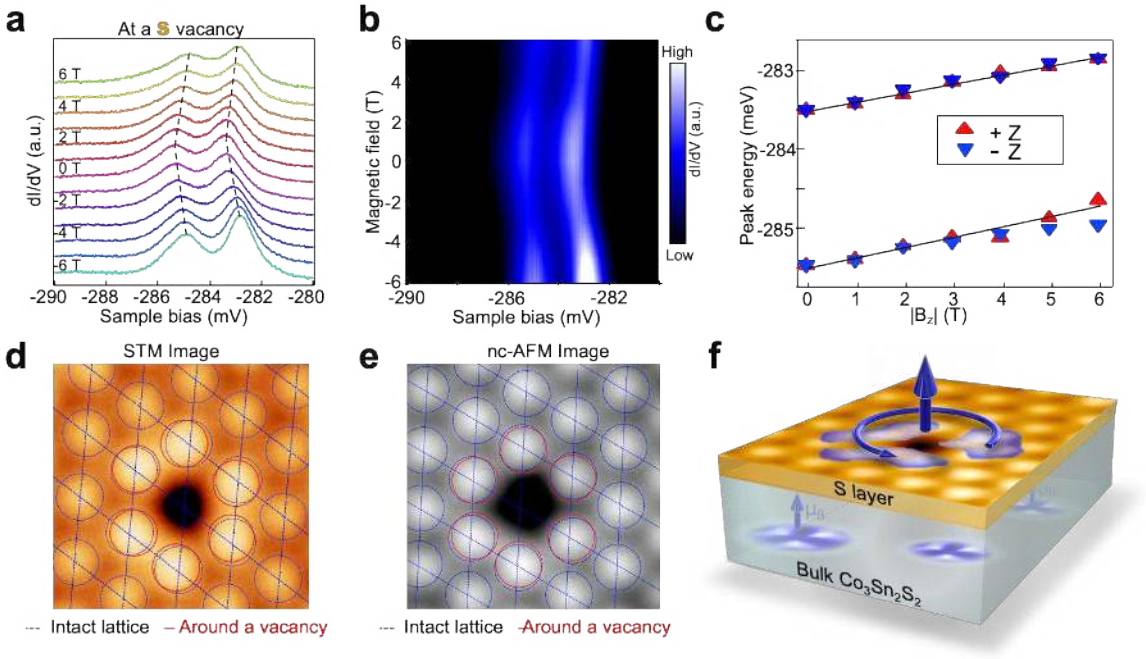

Fig. 4 | Anomalous Zeeman shift of the bound states and spin-orbit polaron at a single S-vacancy. a, dI/dV spectra of the bound states in a magnetic field perpendicular to the sample surface from -6 T to 6 T, showing an approximately linear shift independent of the magnetic field direction. (V_s=-400 mV, I_t=500 pA, V_{mod}=0.5 mV). **b,** Intensity plot of (**a**). **c,** Energy shift of peak positions plotted as a function of the absolute value of magnetic field. **d-e,** STM and nc-AFM images (2.3 nm × 2.3 nm) of the same single S-vacancy, showing appreciable lattice distortion (detailed analysis please refer to Extended Data Fig. 9) around the single S-vacancy (STM: V_s=-400 mV, I_t=500 pA; AFM: Δf = -6 Hz). **f,** Schematic illustration of the localized spin-orbit polaron in $Co_3Sn_2S_2$.

Methods

Single crystal growth of $Co_3Sn_2S_2$

The single crystals of $Co_3Sn_2S_2$ were grown by flux method with Sn/Pb mixed flux. The starting materials of Co (99.95% Alfa), Sn (99.999% Alfa), S (99.999% Alfa) and Pb (99.999% Alfa) were mixed in molar ratio of Co : S : Sn : Pb = 12 : 8 : 35 : 45. The mixture was placed in Al_2O_3 crucible sealed in a quartz tube. The quartz tube was slowly heated to 673 K over 6 h and kept over 6 h to avoid the heavy loss of sulfur. The quartz tube was further heated to 1323 K over 6 h and kept for 6 h. Then the melt was cooled down slowly to 973 K over 70 h. At 973 K, the flux was removed by rapid decanting and subsequent spinning in a centrifuge. The hexagonal-plate single crystals with diameters of 2 ~ 5 mm were obtained. The composition and phase structure of the crystals was checked by energy-dispersive x-ray spectroscopy and x-ray diffraction, respectively.

Scanning tunneling microscopy/spectroscopy

The samples used in the experiments cleaved *in situ* at 6 K and immediately transferred to an STM chamber. Experiments were performed in an ultrahigh vacuum (1×10^{-10} mbar) ultra-low temperature STM system (40 mK) equipped with 9-2-2 T magnetic field. All the scanning parameter (setpoint voltage and current) of the STM topographic images are listed in the captions of the figures. Unless otherwise noted, the differential conductance (dI/dV) spectra were acquired by a standard lock-in amplifier at a modulation frequency of 973.1 Hz. Non-magnetic tungsten tip was fabricated via electrochemical etching and calibrated on a clean Au(111) surface prepared by repeated cycles of sputtering with argon ions and annealing at 500 °C. Ferromagnetic Ni tip was applied in the spin-polarized STM measurement. The Ni tip was fabricated via electrochemical etching of Ni wire in a constant-current mode[41]. To calibrate the spin-polarization of Ni tip, the as-prepared Ni tip has been applied to resolve magnetic-state-dependent contrast of Co islands grown on a Cu(111) surface in spin-polarized STM experiments (details are shown in Extended Data Fig. 5). External magnetic fields of +0.6 T (-0.6 T) were applied to magnetize the Ni tip to be in the spin up (spin down) states. This tip was then used to measure the spin-dependent dI/dV spectra at 0 T on the same atomic location. We also reproduce the spin-polarized measurements result by applying +0.2 T (-0.2 T) external magnetic fields.

Non-contact atomic force microscopy (nc-AFM)

nc-AFM measurements were performed at LHe temperature with the base pressure lower than 2×10^{-10} mbar. All nc-AFM measurements were performed using a commercial qPlus tuning fork sensor in frequency modulation mode with a Pt/Ir tip, while all STM topographic images were simultaneously acquired in constant-current mode. The resonance frequency is about 27.9 kHz, and stiffness about 1800 N/m. The imaging heights for all nc-AFM measurements are reported in figure captions referred to the STM tunneling junction height on clean Ag(100) substrate which is -30 mV and 10 pA. All STM and nc-AFM images were processed using free and open source software Gwyddion.

Density functional theory calculations

Quantum mechanical calculations based on density functional theory (DFT) were performed by using the Vienna Ab initio Simulation Package (VASP)[42,43]. The projector augmented wave (PAW)[44] method was employed, and the Perdew–Burke–Ernzerhof (PBE)[45] type of exchange correlation functional was used.

The slab models containing six Co-Sn layers and extra S or Sn layers were used to simulate the S-terminated and Sn-terminated surfaces. S surfaces with a single S-vacancy were simulated by a 4×4 supercell. In structural relaxation, the atoms in the two middle Co_3Sn layers were fixed, while atoms in other layers were totally relaxed. The vacuum layers of the slab models were larger than 15 Å. A S vacancy in bulk is modeled in a $2 \times 2 \times 2$ supercell.

The wavefunctions were expanded in plane waves with a kinetic energy cutoff of 400 eV. For pristine S-terminated and Sn-terminated surfaces of $Co_3Sn_2S_2$, the k-points sampling was $8 \times 8 \times 1$, generated by Monkhorst-Pack grids with the origin at the Γ-point. The structures were relaxed until the energy and residual force on each atom were smaller than 10^{-6} eV and 0.001 eV/Å, respectively. For S-terminated surface with a single vacancy, the k-points sampling was with only the Γ-point. For the S vacancy in bulk, the k-points sampling was $3 \times 3 \times 3$, generated by Monkhorst-Pack grids with the origin at the Γ-point. The structures were relaxed until the energy and residual force on each atom were smaller than 10^{-4} eV and 0.01 eV/Å, respectively. Non-collinear calculations considering the spin-orbit coupling (SOC) were carried out to determine the magnetic moment direction of each layers. It is found that for the slab model calculations, the easy axis is in the z (out of plane) direction.

With these parameters, the optimized lattice constants of bulk $Co_3Sn_2S_2$ are 5.37 Å and 13.15 Å along *a* and *c* directions, respectively. The magnetic moment is 0.35 μ_B, -0.02 μ_B, -0.03 μ_B, and 0 μ_B for Co, Sn in Co_3Sn plan, Sn in Sn layer, and S, respectively**.** The magnetic moment and projected density of states of the polaron were calculated by projecting the wave function onto an empty sphere sitting at the S vacancy site. The radius of this sphere is chosen as 1.164 Å, which is the Wigner-Seitz radius of S.

References

1. Xu, G., Weng, H., Wang, Z., Dai, X. & Fang, Z. Chern semimetal and the quantized anomalous Hall effect in $HgCr_2Se_4$. *Phys. Rev. Lett.* **107**, 186806 (2011).
2. Burkov, A. A. & Balents, L. Weyl semimetal in a topological insulator multilayer. *Phys. Rev. Lett.* **107**, 127205 (2011).
3. Wan, X., Turner, A. M., Vishwanath, A. & Savrasov, S. Y. Topological semimetal and Fermi-arc surface states in the electronic structure of pyrochlore iridates. *Phys. Rev. B* **83**, 205101 (2011).
4. Wang, Z. *et al.* Time-reversal-breaking Weyl fermions in magnetic heusler alloys. *Phys. Rev. Lett.* **117**, 236401 (2016).
5. Ye, L. *et al.* Massive Dirac fermions in a ferromagnetic kagome metal. *Nature* **555**, 638–642 (2018).
6. Yin, J.-X. *et al.* Giant and anisotropic many-body spin–orbit tunability in a strongly correlated kagome magnet. *Nature* **562**, 91–95 (2018).
7. Yang, R. *et al.* Magnetization-induced band shift in ferromagnetic Weyl semimetal $Co_3Sn_2S_2$. *Phys. Rev. Lett.* **124**, 077403 (2020).
8. Liu, E. *et al.* Giant anomalous Hall effect in a ferromagnetic kagome-lattice semimetal. *Nat. Phys.* **14**, 1125–1131 (2018).
9. Wang, Q. *et al.* Large intrinsic anomalous Hall effect in half-metallic ferromagnet $Co_3Sn_2S_2$ with magnetic Weyl fermions. *Nat. Commun.* **9**, 3681 (2018).
10. Liu, D. F. *et al.* Magnetic Weyl semimetal phase in a kagomé crystal. *Science* **365**, 1282–1285 (2019).
11. Morali, N. *et al.* Fermi-arc diversity on surface terminations of the magnetic Weyl semimetal $Co_3Sn_2S_2$. *Science* **365**, 1286–1291 (2019).
12. Guin, S. N. *et al.* Zero-field Nernst effect in a ferromagnetic kagome-lattice Weyl-semimetal $Co_3Sn_2S_2$. *Adv. Mater.* **31**, 1806622 (2019).
13. Li, G. *et al.* Surface states in bulk single crystal of topological semimetal $Co_3Sn_2S_2$ toward water oxidation. *Sci. Adv.* **5**, eaaw9867 (2019).
14. Yin, J.-X. *et al.* Negative flat band magnetism in a spin–orbit-coupled correlated kagome magnet. *Nat. Phys.* **15**, 443–448 (2019).
15. Bode, M. *et al.* Chiral magnetic order at surfaces driven by inversion asymmetry. *Nature* **447**, 190–193 (2007).
16. Khajetoorians, A. A. *et al.* Detecting excitation and magnetization of individual dopants in a semiconductor. *Nature* **467**, 1084–1087 (2010).
17. Gambardella, P. *et al.* Ferromagnetism in one-dimensional monatomic metal chains. *Nature* **416**, 301–304 (2002).
18. Kubodera, T., Okabe, H., Kamihara, Y. & Matoba, M. Ni substitution effect on magnetic and transport properties in metallic ferromagnet. *Physica B: Condensed Matter* **378–380**, 1142–1143 (2006).
19. Schnelle, W. *et al.* Ferromagnetic ordering and half-metallic state of $Sn_2Co_3S_2$ with the shandite-type structure. *Phys. Rev. B* **88**, 144404 (2013).
20. Jiao, L. *et al.* Signatures for half-metallicity and nontrivial surface states in the kagome lattice Weyl semimetal $Co_3Sn_2S_2$. *Phys. Rev. B* **99**, 245158 (2019).
21. Howard, S. *et al.* Observation of linearly dispersive edge modes in a magnetic Weyl semimetal $Co_3Sn_2S_2$. *Preprint at: arXiv:1910.11205 (2019)*.

22. Giessibl, F. J. Atomic resolution on Si(111)-(7×7) by noncontact atomic force microscopy with a force sensor based on a quartz tuning fork. *Appl. Phys. Lett.* **76**, 1470–1472 (2000).
23. Gross, L. *et al.* Measuring the charge state of an adatom with noncontact atomic force microscopy. *Science* **324**, 1428–1431 (2009).
24. Melitz, W., Shen, J., Kummel, A. C. & Lee, S. Kelvin probe force microscopy and its application. *Surf. Sci. Rep.* **66**, 1–27 (2011).
25. Oka, H. *et al.* Spin-polarized quantum confinement in nanostructures: Scanning tunneling microscopy. *Rev. Mod. Phys.* **86**, 1127–1168 (2014).
26. Chen, W. *et al.* Direct observation of van der Waals stacking–dependent interlayer magnetism. *Science* **366**, 983–987 (2019).
27. Zhang, S.-F., Zhang, C.-W., Wang, P.-J. & Sun, Q.-F. Low-energy electronic properties of a Weyl semimetal quantum dot. *Sci. China Phys. Mech. Astron.* **61**, 117811 (2018).
28. Furdyna, J. K. Diluted magnetic semiconductors. *J. Appl. Phys.* **64**, R29 (1988).
29. Dietl, T. in *Handbook on Semiconductors* vol. 3b 1251 (North-Holland, Amsterdam, 1994).
30. Dietl, T., Ohno, H. & Matsukura, F. Hole-mediated ferromagnetism in tetrahedrally coordinated semiconductors. *Phys. Rev. B* **63**, 195205 (2001).
31. Wolff, P. A., Bhatt, R. N. & Durst, A. C. Polaron-polaron interactions in diluted magnetic semiconductors. *J. Appl. Phys.* **79**, 5196 (1996).
32. Kaminski, A. & Das Sarma, S. Polaron percolation in diluted magnetic semiconductors. *Phys. Rev. Lett.* **88**, 247202 (2002).
33. He, M. *et al.* Polaronic transport and magnetism in Ag-doped ZnO. *Appl. Phys. Lett.* **99**, 222511 (2011).
34. Dedkov, Y. S., Holder, M., Molodtsov, S. L. & Rosner, H. Electronic structure of shandite $Co_3Sn_2S_2$. *J. Phys.: Conf. Ser.* **100**, 072011 (2008).
35. Entin-Wohlman, O., Imry, Y., Aronov, A. G. & Levinson, Y. Orbital magnetization in the hopping regime. *Phys. Rev. B* **51**, 11584–11596 (1995).
36. Liu, Q., Liu, C.-X., Xu, C., Qi, X.-L. & Zhang, S.-C. Magnetic impurities on the surface of a topological insulator. *Phys. Rev. Lett.* **102**, 156603 (2009).
37. Potasz, P. & Fernández-Rossier, J. Orbital magnetization of quantum spin Hall insulator nanoparticles. *Nano Lett.* **15**, 5799–5803 (2015).
38. Wilson, J. H., Pixley, J. H., Huse, D. A., Refael, G. & Das Sarma, S. Do the surface Fermi arcs in Weyl semimetals survive disorder? *Phys. Rev. B* **97**, 235108 (2018).
39. Sakai, Y. *et al.* Magnetic properties of Shandite-phase $Co_{3-x}Fe_xSn_2S_2$(x=0-1.0) obtained with high pressure synthesis. *J. Phys. Soc. Jpn.* **84**, 044705 (2015).
40. Lühmann, T., John, R., Wunderlich, R., Meijer, J. & Pezzagna, S. Coulomb-driven single defect engineering for scalable qubits and spin sensors in diamond. *Nat. Commun.* **10**, 4956 (2019).
41. Chen, H., Xiao, W., Wu, X., Yang, K. & Gao, H.-J. Electrochemically etched Ni tips in a constant-current mode for spin-polarized scanning tunneling microscopy. *J. Vac. Sci. Tech. B* **32**, 061801 (2014).
42. Kresse, G. & Furthmüller, J. Efficiency of ab-initio total energy calculations for metals and semiconductors using a plane-wave basis set. *Comput. Mat. Sci.* **6**, 15–50 (1996).
43. Kresse, G. & Furthmüller, J. Efficient iterative schemes for *ab initio* total-energy calculations using a plane-wave basis set. *Phys. Rev. B* **54**, 11169–11186 (1996).
44. Blöchl, P. E. Projector augmented-wave method. *Phys. Rev. B* **50**, 17953–17979 (1994).
45. Perdew, J. P., Burke, K. & Ernzerhof, M. Generalized gradient approximation made simple. *Phys. Rev. Lett.* **78**, 1396–1396 (1997).

46. Wiesendanger, R. Spin mapping at the nanoscale and atomic scale. *Rev. Mod. Phys.* **81**, 1495–1550 (2009).
47. Pietzsch, O., Kubetzka, A., Bode, M. & Wiesendanger, R. Spin-polarized scanning tunneling spectroscopy of nanoscale cobalt Islands on Cu(111). *Phys. Rev. Lett.* **92**, 057202 (2004).

Acknowledgements
We thank Qing-Feng Sun, Fu-Chun Zhang, Gang Su, and Werner Hofer for helpful discussions. The work is supported by grants from the National Natural Science Foundation of China (61888102 and 11974394), the National Key Research and Development Projects of China (2016YFA0202300, 2017YFA0206303, 2018YFA0305800 and 2019YFA0308500), and the Chinese Academy of Sciences (XDB28000000, 112111KYSB20160061). Z.Q.W. is supported by the US DOE, Basic Energy Sciences Grant No. DE-FG02-99ER45747.

Author Contributions: H.-J.G. designed the experiments. Y.X., H.C. and B.H. performed STM experiments with guidance of H.-J.G. L.H., Q.Z., R.S. Ma, and L.X. performed AFM/STM experiments. E.L., J.S., Q.W., Q.Y., H.L. and B.S. prepared samples. Z.W. proposed the model and Y.G., X.Z., Y.Y.Z., S.D. and W.J. carried out theoretical calculations. All of the authors participated in analyzing experimental data, plotting figures, and writing the manuscript. H.-J. G. and Z.W. supervised the project.

Competing interests: The authors declare that they have no competing interests.

Extended Data Figures for

Localized spin-orbit polaron in magnetic Weyl semimetal $Co_3Sn_2S_2$

Yuqing Xing[1,2,3†], Jianlei Shen[1,2†], Hui Chen[1,2,3†], Li Huang[1,2,3†], Yuxiang Gao[1,2,3], Qi Zheng[1,2,3], Yu-Yang Zhang[2,3], Geng Li[1,2,3], Bin Hu[1,2,3], Guojian Qian[1,2,3], Lu Cao[1,2,3], Xianli Zhang[1,2,3], Peng Fan[1,2,3], Ruisong Ma[1,2,3],Qi Wang[4], Qiangwei Yin[4], Hechang Lei[4], Wei Ji[4], Shixuan Du[1,2,3,5], Haitao Yang[1,2,3], Chengmin Shen[1,2,3], Xiao Lin[2,1,3], Enke Liu[1,2,5], Baogen Shen[1,2], Ziqiang Wang[6*], and Hong-Jun Gao[1,2,3,5*]*

[1] *Beijing National Center for Condensed Matter Physics and Institute of Physics, Chinese Academy of Sciences, Beijing 100190, PR China*

[2] *School of Physical Sciences, University of Chinese Academy of Sciences, Beijing 100190, PR China*

[3] *CAS Center for Excellence in Topological Quantum Computation, University of Chinese Academy of Sciences, Beijing 100190, PR China*

[4] *Beijing Key Laboratory of Optoelectronic Functional Materials & Micro-Nano Devices, Department of Physics, Renmin University of China, Beijing 100872, PR China*

[5] *Songshan Lake Materials Laboratory, Dongguan, Guangdong 523808, PR China*

[6] *Department of Physics, Boston College, Chestnut Hill, MA, USA*

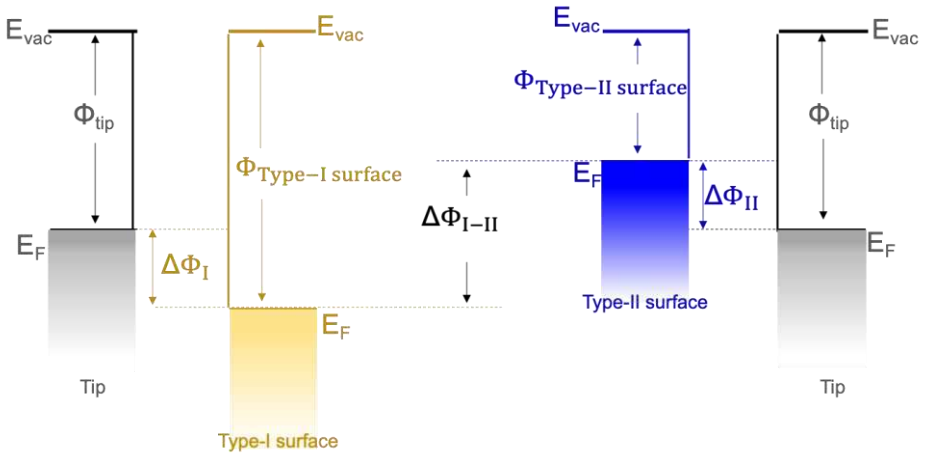

Extended Data Fig. 1 | Schematic of the relationship between work function and local contact potential difference (LCPD) (V_{CPD}) of the Type-I and the Type-II surfaces, respectively. $V_{\mathrm{CPD}} = \frac{\Phi_{\mathrm{tip}}-\Phi_{\mathrm{sample}}}{-e}$. eV_{CPD} is the difference of the work function between the sample surface and tip. Φ_{tip} is the work function of the tip, $\Phi_{\mathrm{Type-I\ surface}}$ the work function of the Type-I surface, $\Phi_{\mathrm{Type-II\ surface}}$ the work function of the Type-II surface. Based on the nc-AFM measurements shown in the Fig. 1g of main text, we got: $\Delta\Phi_{\mathrm{I}} = \Phi_{\mathrm{tip}} - \Phi_{\mathrm{type-I\ surface}} = -eV_{CPD}^{I} = 0.22$ eV; $\Delta\Phi_{\mathrm{II}} = \Phi_{\mathrm{tip}} - \Phi_{\mathrm{type-II\ surface}} = -eV_{CPD}^{II} = -0.57$ eV; Thus, $\Delta\Phi_{\mathrm{I-II}} = \Delta\Phi_{\mathrm{I}} - \Delta\Phi_{\mathrm{II}} = 0.79$ eV.

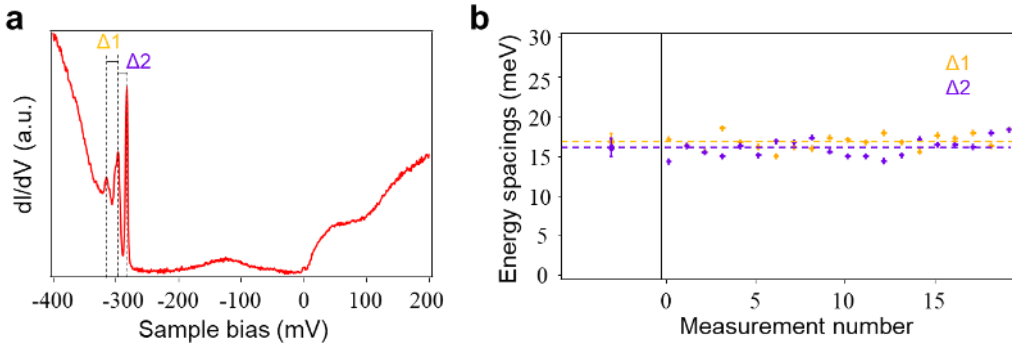

Extended Data Fig. 2 | Energy spacing of the bound states obtained at single S-vacancy. a, Typical dI/dV spectrum obtained at a single S-vacancy (V_s=-400 mV, I_t=500 pA, V_{mod}=0.5 mV), which is highly reproducible for different samples and STM tips. The energy spacings are labelled as Δ1 and Δ2 in (**a**). **b,** Yellow and the purple dots in the left panel represent the average energy spacing of Δ1 and Δ2, respectively. All the individual reproducible measurements are displayed in the right panel, indicating that the peak energies are equally spaced.

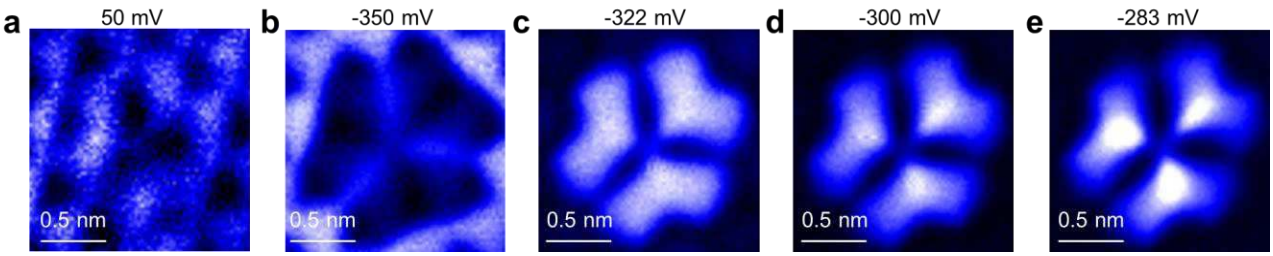

Extended Data Fig. 3 | dI/dV map in Fig. 2. a-e, dI/dV maps of single S-vacancy at different sample bias: 50 mV (**a**), -350 mV (**b**), -322 mV (**c**), -300 mV (**d**), and -283 mV (**e**), respectively.

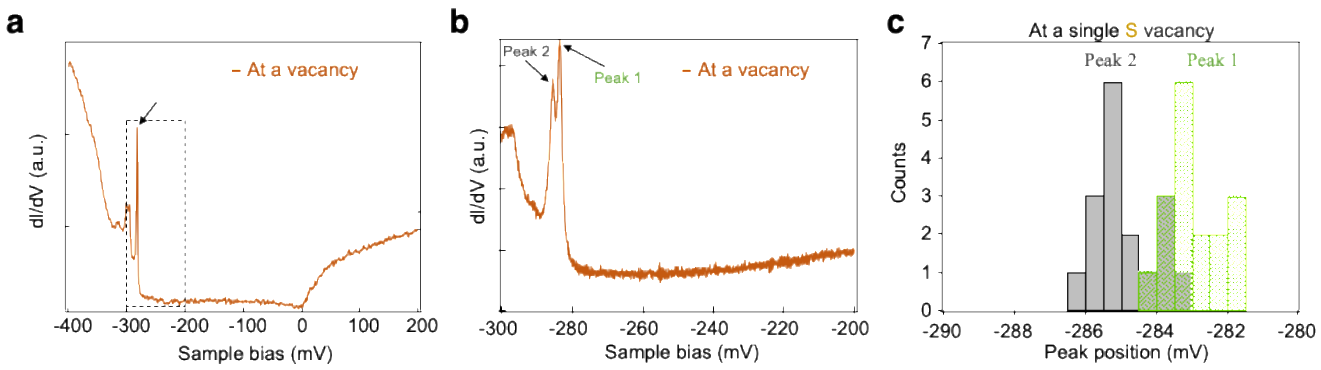

Extended Data Fig. 4 | Two-peak feature of dI/dV spectra obtained on a single S-vacancy site. a, dI/dV spectra at a single S-vacancy (V_s=-400 mV, I_t=500 pA, V_{mod}=0.5 mV). **b,** Zoom-in of (**a**), ranging from -300 mV to -200 mV, showing a two-peak feature near -283 mV (V_s=-300 mV, I_t=500 pA, V_{mod}=0.5 mV), possibly due to the exchange field induced energy splitting. **c,** Two sets of energy peaks obtained from 17 different single-S vacancies show a similar variation of ±1.5 mV, indicating that the bound states are robust at the single S-vacancy sites.

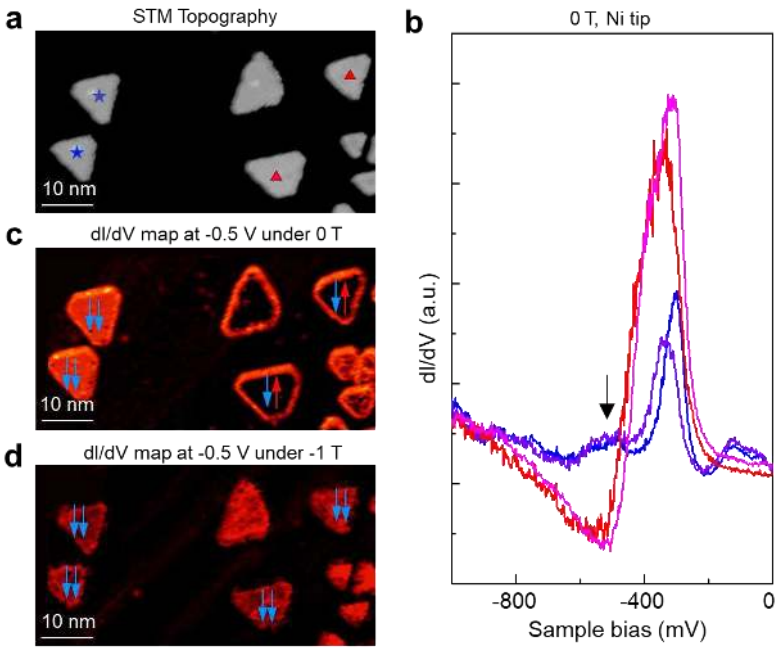

Extended Data Fig. 5 | Calibration of spin-polarized Ni tip on Co/Cu(111). a, STM image, showing the topography of Co islands on Cu(111). (V_s=-400 mV, I_t=100 pA). **b,** dI/dV spectra obtained on four Co islands with the same stack configurations using the Ni tip. The blue and purple curves are obtained on the blue and purple stars in (**a**), the pink and red curve are obtained on pink and red triangles in (**a**). **c-d**, dI/dV map of (**a**) at the energy of -0.5 V at magnetic field of 0 T (**c**) and -1 T (**d**). The contrast on the same stacked islands at 0 T and the absence of contrast at -1 T confirm the spin-polarization of the Ni tip[46,47]. The spin orientations of the Co island and tip are labelled by the upward (red) or downward (blue) arrows.

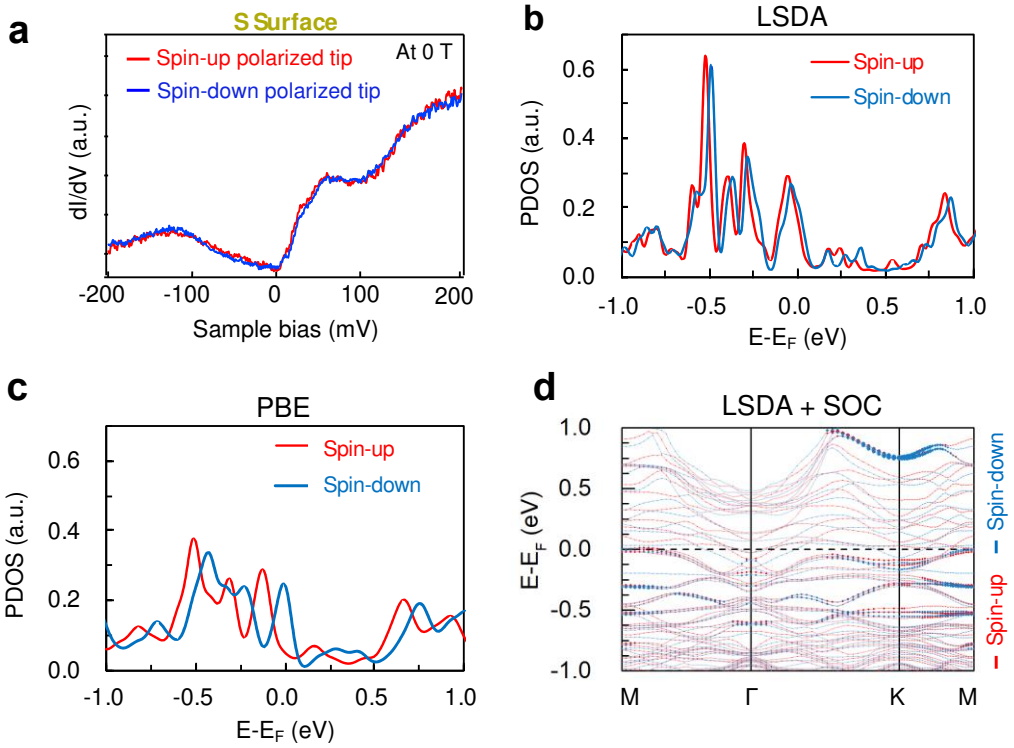

Extended Data Fig. 6 | Spin-polarized dI/dV spectra and calculated PDOS of the S-terminated surface. a, Spin polarized dI/dV spectrum of the S-terminated surface (same as Fig. 3a). **b,** Spin-resolved density of state (DOS) projected on a surface S atom of the S-terminated surface with LSDA functional. The DOS curves of the two spins of S surface are almost degenerate. The net magnetic moment of the S atom is 0.003 μB**. c,** Spin-resolved density of state (DOS) projected on a surface S atom of the S-terminated surface with PBE functional. The DOS curves of the two spins of S surface show similar shapes but with a ~ 0.2 eV energy shift. The net magnetic moment of the S atom is 0.005 μ_B. **d,** The energy bands projected on the S surface calculated with LSDA functional and spin-orbital coupling.

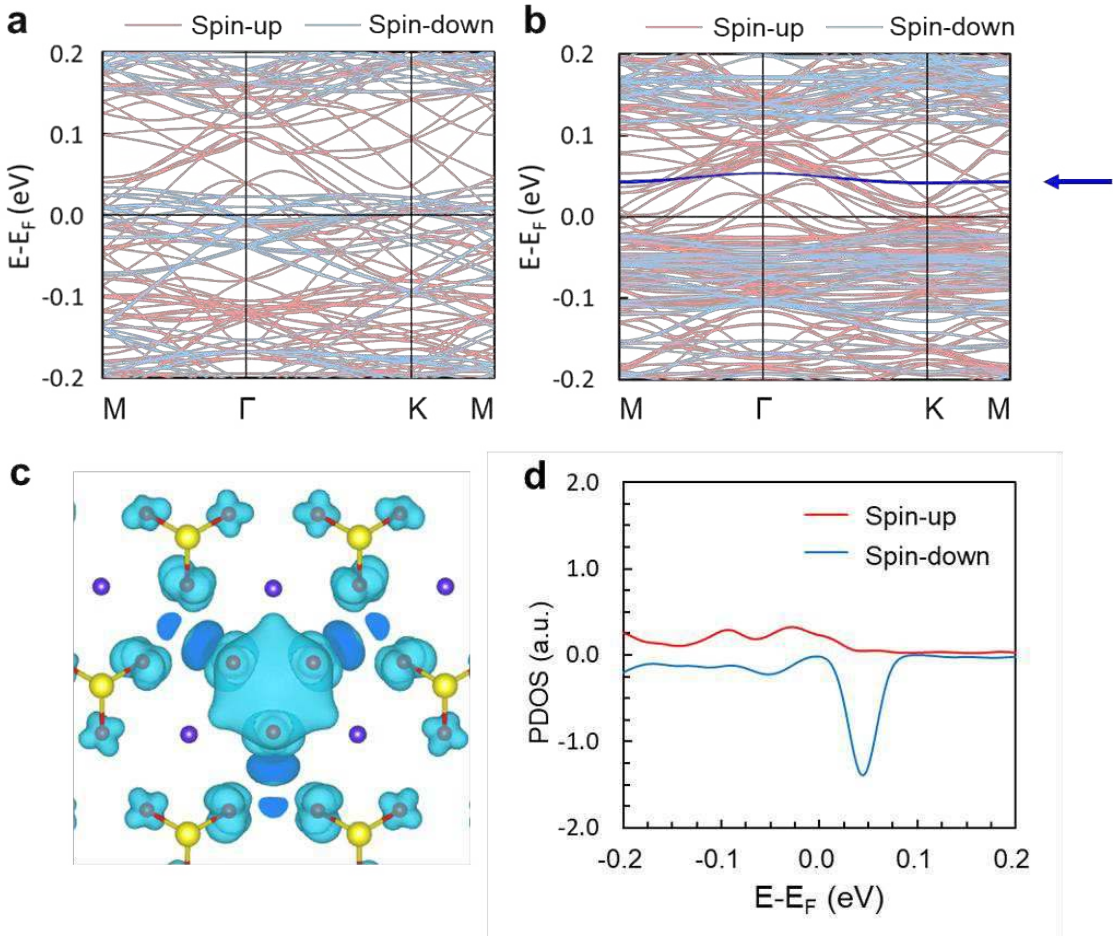

Extended Data Fig. 7 | Calculated electronic structures of the pristine and defective (with a S vacancy) S-terminated surfaces. Band structures of the pristine (**a**) and the defective (**b**) S surface (in a 4 × 4 supercell). By comparing (**a**) and (**b**), a bound state is clearly visible as marked by the blue solid line and labelled by the blue arrow in (**b**). **c,** Spatial distribution of the wavefunction norm of the bound state marked in (**b**), which confirms its bound state nature. An isosurface of 3.0×10^{-4} e/Bohr^3 is used. **d,** Spin-resolved DOS projected on the S vacancy, showing appreciable spin-polarization, in agreement with the experimental observation. We want to point out that the bound state is almost two-fold degenerated, while there are at least three bound states observed experimentally. The experiment-theory discrepancy reflects the limitation of standard DFT to explain the defect excitations in magnetic Weyl semimetals. The magnetic moment integrated within the sphere of radius 1.164 Å (the Wigner-Seitz radius of S atom) is 0.04 μ_B. The experimental data (Fig. 2d-h) indicate that the size of the localized polaron is much larger and contains a cluster of atoms around the S vacancy. Therefore we estimate the contribution to the magnetic moment of the localized polaron from one S vacancy and three neighboring Co atoms. The total

pseudospin (electron spin + atomic orbital) magnetic moment from the calculation is 0.85 μ_B. For the three Co atoms nearest to S vacancy, the orbital moment is 0.09 μ_B and the total magnetic moment is 0.81 μ_B. In the standard formula of DFT for non-collinear spin calculations, the diamagnetic term of the Dirac equation is ignored, which cannot account for the diamagnetic orbital magnetization contribution. This paramagnetic spin-orbit moment follows the magnetic field direction and cannot explain the observed net diamagnetic moment of 1.35 μ_B that always points in the opposite direction of the magnetic field. The exact diamagnetic orbital moment thus equals to the value of the net diamagnetic moment plus that of the paramagnetic moment revealed by DFT, i.e. being of the order ~ (1.35 + 0.85) =2.20 μ_B. The discrepancy on diamagnetic moment between our experiment and DFT calculation, indeed, supports the spin-orbit nature of the found polaron.

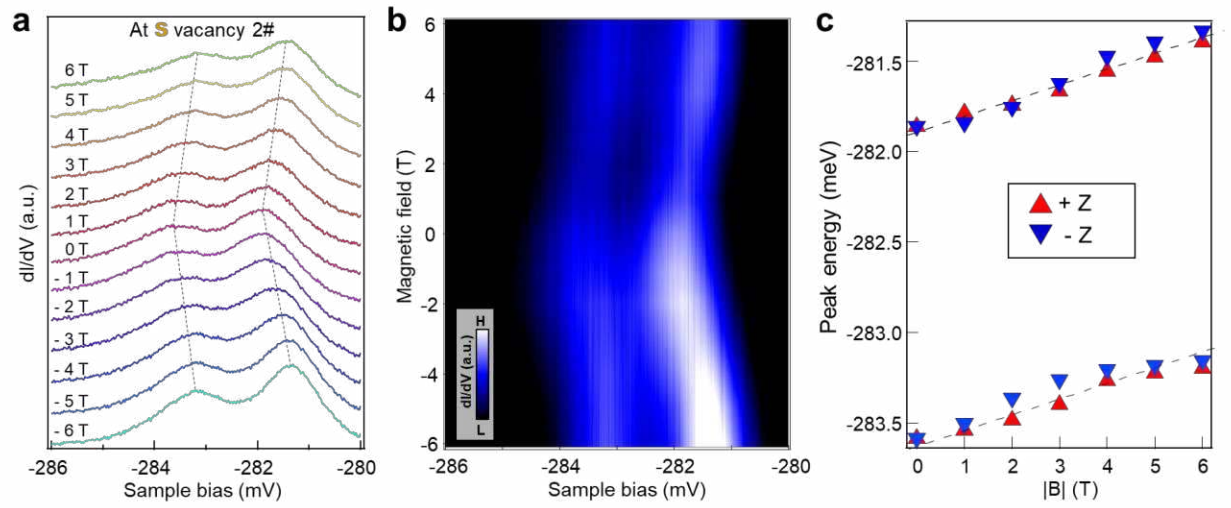

Extended Data Fig. 8 | Anomalous Zeeman shift of the SOP under external magnetic fields. This set of data is taken on another single S-vacancy, showing the reproducibility of the results in Fig. 4a-c. **a,** Magnetic field dependence of the peak positions on a single S-vacancy (V_s=-400 mV, I_t=500 pA, V_{mod}=0.5 mV). **b,** Intensity plot of the interpolated field-dependent spectra, showing a similar shift as that in (**a**). **c,** Peak energy as a function of the absolute value of the external magnetic field in (**a**).

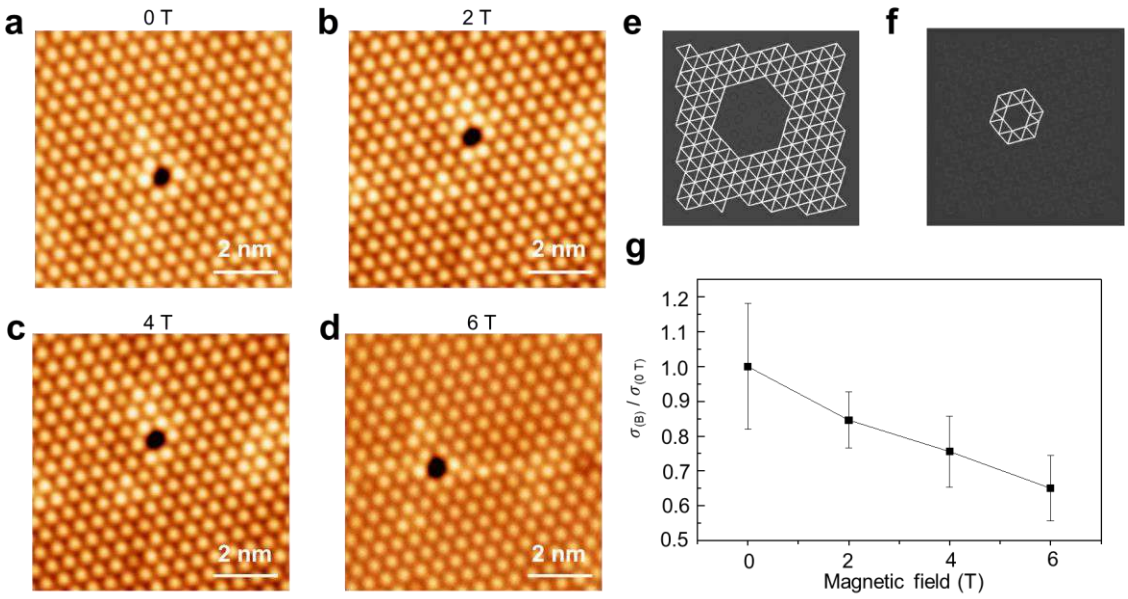

Extended Data Fig. 9 | Statistical analysis of magnetic-field-dependent local atomic displacement induced by a single S-vacancy. a-d, STM images of a single S-vacancy obtained under 0 T (**a**), 2 T (**b**), 4 T (**c**), and 6 T (**d**), respectively (V_s=-400 mV, I_t=100 pA). **e**, An example of extracted nearest neighbor distances in the region far away from the vacancy in (**c**). The average distance is regarded as the standard atom-atom distance $\bar{d}$. **f,** An example of extracted nearest neighbor distances (d_i, i=1, 2, 3…, 36) in the region of the vacancy in (**c**), according to the dI/dV map of vacancy in Fig. 2h in the main text. The center position of single atom was obtained by fitted the STM image with bivariate normal distribution:

$$f(x,y) = C_1 + \frac{C_2}{2\pi\sigma_X\sigma_Y\sqrt{1-\rho^2}}\exp\left(-\frac{1}{2(1-\rho^2)}\left[\frac{(x-\mu_X)^2}{\sigma_X^2}+\frac{(y-\mu_Y)^2}{\sigma_Y^2}-\frac{2\rho(x-\mu_X)(y-\mu_Y)}{\sigma_X\sigma_Y}\right]\right)$$

Where C_1 and C_2 are fitting constants, σ_X and σ_Y are the standard deviation of the distribution along x and y direction, respectively, ρ is the correlation between x and y direction, and (μ_X, μ_Y) is the expectation of the distribution, i.e. the position of atom. The local atomic displacement of a single S-vacancy σ is defined as $\sigma = \sqrt{\sum_{i=1}^{36}\frac{(d_i-\bar{d})^2}{36\bar{d}}}$. **g,** The local atomic displacement as a function of the magnetic field strength, showing that the displacement decreases with increasing magnetic field. The error bars reflect the variation in the determination of the atomic position and in the calculation of the nearest neighbor atom-atom distances.

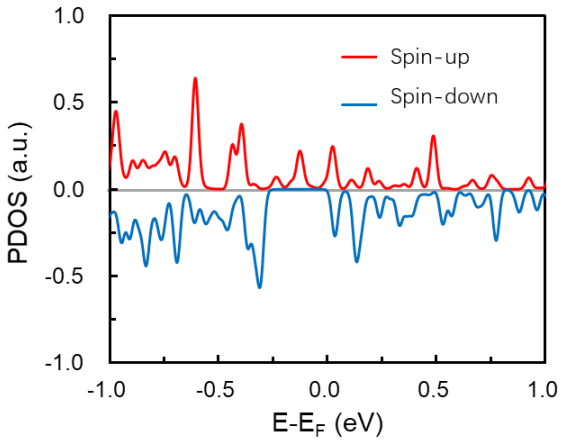

Extended Date Fig. 10 | Density of states projected onto a S vacancy site in a (2×2×2) bulk supercell. It is clearly shown that the S vacancy in bulk $Co_3Sn_2S_2$ is magnetic. The magnetic moment integrated within a S vacancy site is 0.04 μ_B. The existence of S vacancies in bulk also increases the magnetic moment of each nearby Co atom from 0.35 μ_B to 0.72 μ_B.

Figures

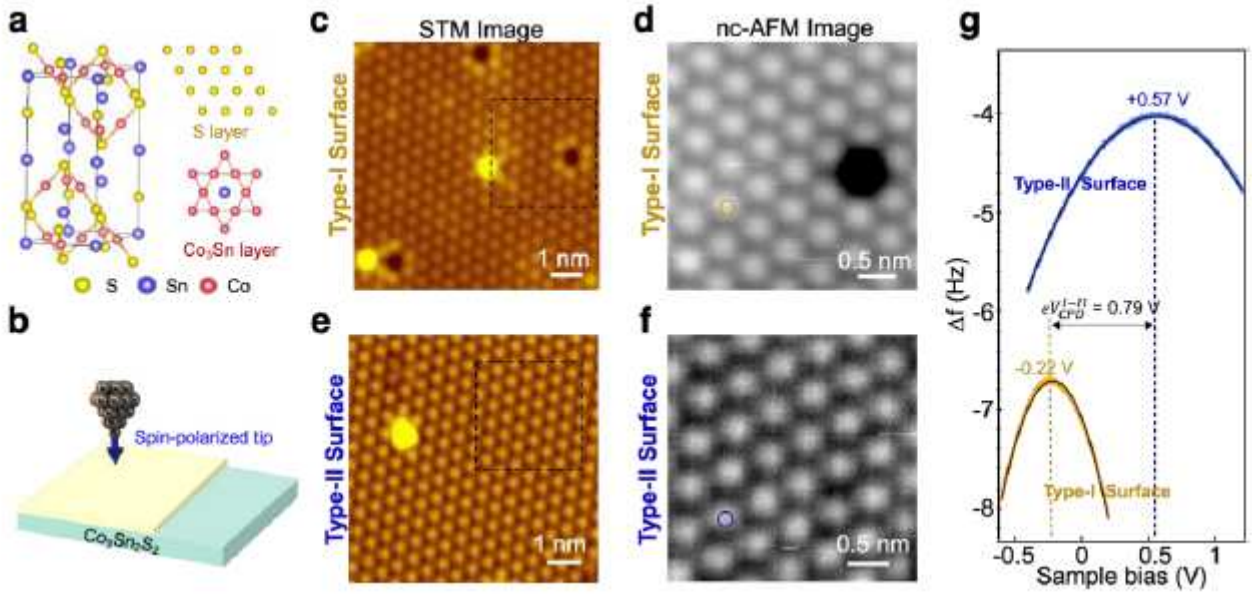

Figure 1

Identification of S-surface of Co3Sn2S2 using nc-AFM/STM. a, Atomic structure of Co3Sn2S2. b, Schematic of spin-polarized STM measurements. c and e, STM images on Type-I and Type-II surfaces, respectively. d and f, Zoomed-in nc-AFM images of (a) and (c) marked by black squares, respectively. g, Δf(V) curves on the orange and blue circles in (d) and (f). The maxima of the Δf(V) parabolas are located at -0.22 V and +0.57 V for Type-I and Type-II surfaces, respectively. The work function difference between the two surfaces is 0.79 eV (refer to Extended Data Fig. 1 for more information). (STM scanning parameters: bias: Vs= -400 mV, setpoint: It= 10 pA); AFM scanning parameters: amplitude= 100 pm, frequency shift Δf = -10 Hz for d and -40 Hz for f).

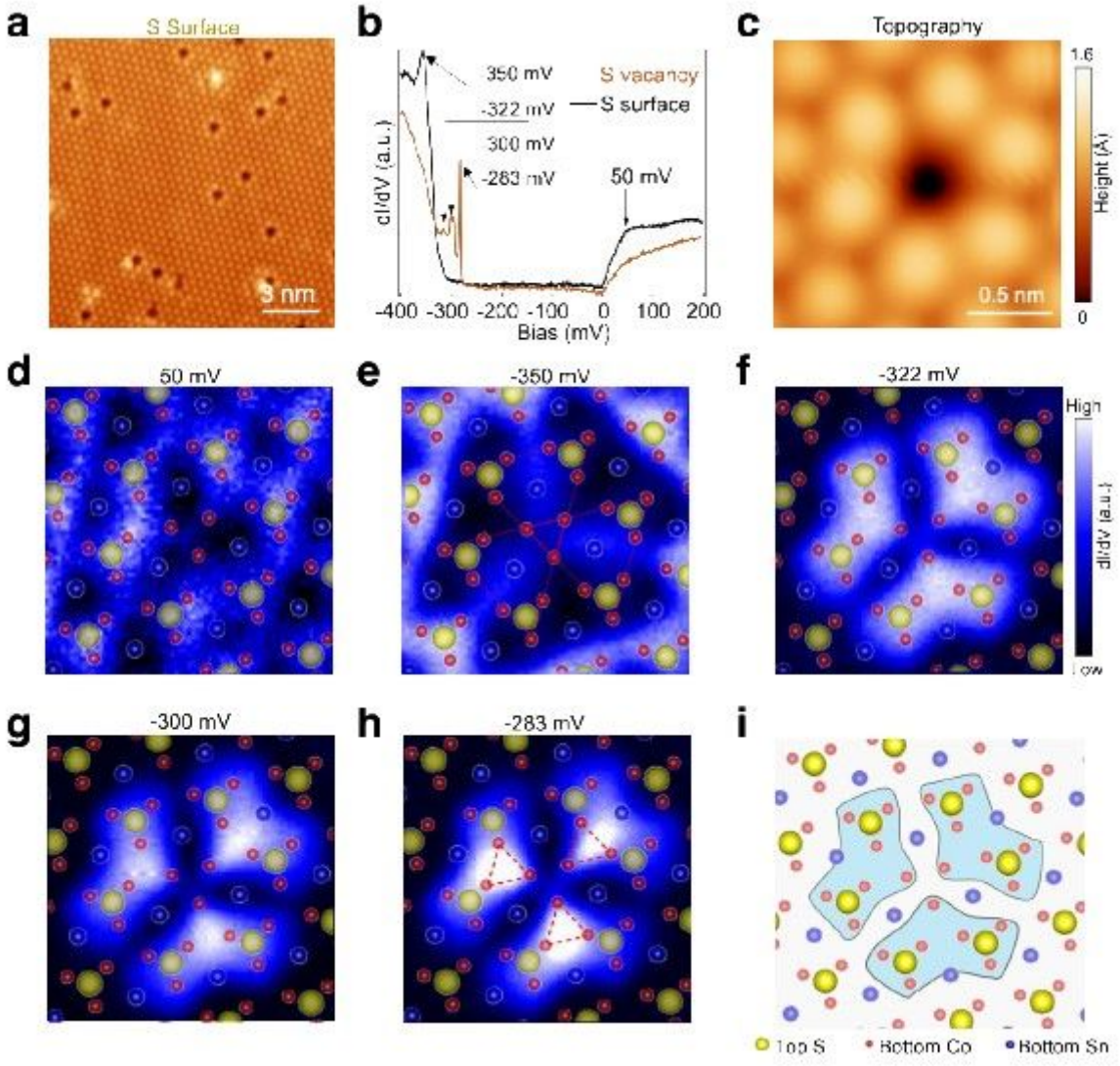

Figure 2

Localized excitations around a single S-vacancy at the S-terminated surface of Co3Sn2S2. a, Atomic-resolution STM image of the S-terminated surface, showing randomly distributed single vacancies (scanning setting: bias: Vs=-400 mV, setpoint It=100 pA). b, dI/dV spectra at (orange curve) and off (black curve) a single S-vacancy (Vs=-400 mV, It=500 pA, Vmod=0.5 mV). c, An STM image of a S-vacancy (Vs=-400 mV, It=500 pA). d-h, dI/dV maps of (c) at different energies: 50 meV (d), -350 meV (e), -322 meV (f), -300 meV (g), and -283 meV (h), respectively. Atomic structure of Co3Sn2S2 is overlaid on each map, showing the correlation between the atomic structure and pattern in dI/dV map (Vs=-400 mV, It=500 pA, Vmod=0.5 mV). i, Correlation between the atomic structure and the pattern in the dI/dV map in (h), showing that the spatial distribution of bound states is correlated to the underlying Co atoms.

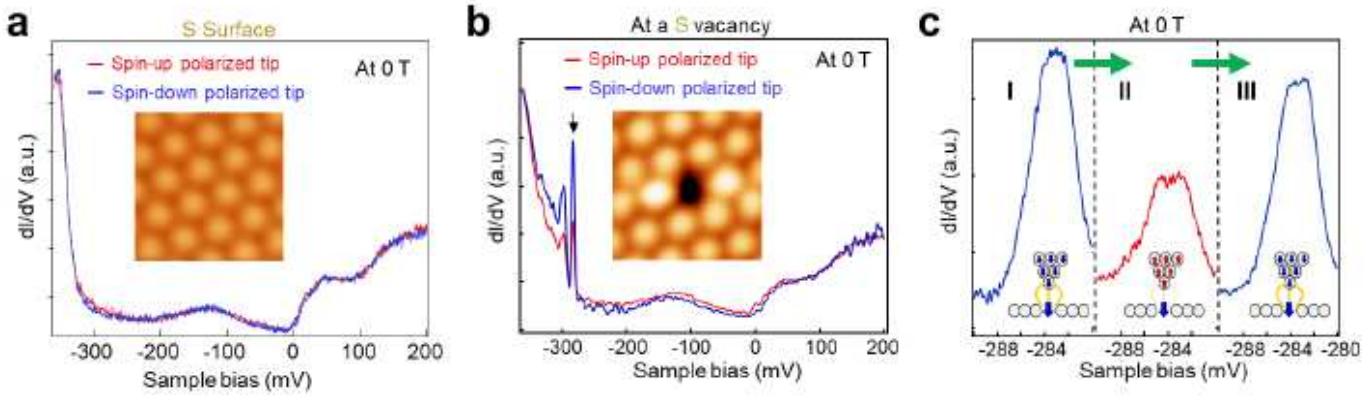

Figure 3

Spin-polarized bound states at a single S-vacancy. a, Spin-polarized dI/dV spectra at the vacancy-free region on S-terminated surface using up-polarized tip (red curve) and down-polarized tip (blue curve), showing nearly no polarization contrast on pristine S-termined surface (Vs=-400 mV, It=100 pA, Modulation Vmod= 0.5 mV). The inset shows the STM image (2 nm × 2 nm) of pristine S-terminated surface. b, dI/dV spectra at the center of a single S-vacancy, showing a spin-down majority behavior. The inset shows the STM image (2 nm × 2 nm) of the single S-vacancy (Vs=-400 mV, It=200 pA, Vmod=0.5 mV). c, Spin-flip operation of the STM tip and the reproducible spectra at the S vacancy site. Left curve (curve I) corresponds to the initial spin-down tip polarization, the middle one (curve II) corresponds to spin-up tip polarization induced by a magnetic field, and the right one (curve III) corresponds to flipping the spin of the tip back to the initial spin-down polarization. (Vs=-400 mV, It=500 pA, Vmod=0.5 mV).

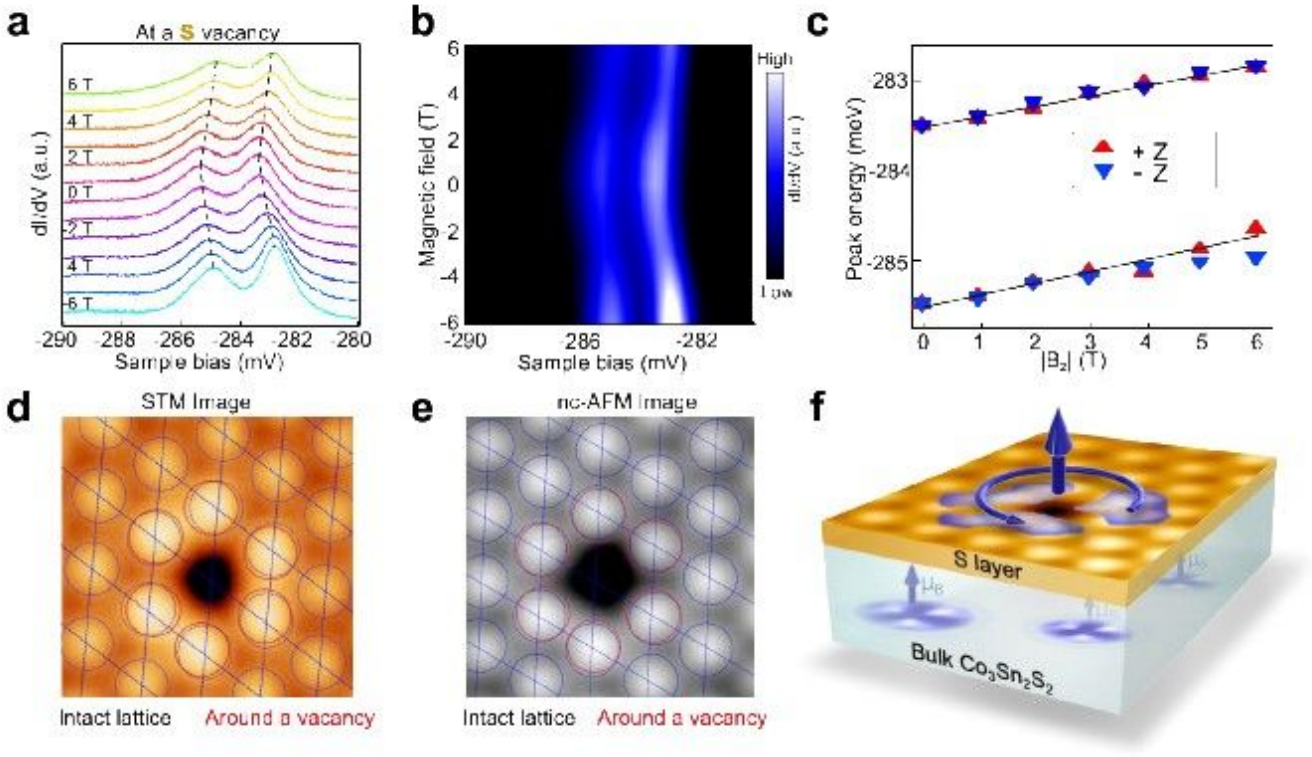

Figure 4

Anomalous Zeeman shift of the bound states and spin-orbit polaron at a single S-vacancy. a, dI/dV spectra of the bound states in a magnetic field perpendicular to the sample surface from -6 T to 6 T, showing an approximately linear shift independent of the magnetic field direction. (Vs=-400 mV, It=500 pA, Vmod=0.5 mV). b, Intensity plot of (a). c, Energy shift of peak positions plotted as a function of the absolute value of magnetic field. d-e, STM and nc-AFM images (2.3 nm × 2.3 nm) of the same single S-vacancy, showing appreciable lattice distortion (detailed analysis please refer to Extended Data Fig. 9) around the single S-vacancy (STM: Vs=-400 mV, It=500 pA; AFM: Δf = -6 Hz). f, Schematic illustration of the localized spin-orbit polaron in Co3Sn2S2.

Supplementary Files

This is a list of supplementary files associated with this preprint. Click to download.

- FigureS1.jpg
- FigureS2.jpg
- FigureS3.jpg
- FigureS4.jpg
- FigureS5.jpg
- FigureS6.jpg
- FigureS7.jpg
- FigureS8.jpg
- FigureS9.jpg
- FigureS10.jpg